

Near-Resonance Spontaneous-Spin-Flip Light Scattering in InSb[†]

S. R. J. Brueck, A. Mooradian, and F. A. Blum*

Lincoln Laboratory, Massachusetts Institute of Technology, Lexington, Massachusetts 02173

(Received 2 January 1973)

The properties of near-resonance spontaneous-spin-flip Raman scattering in InSb have been studied both experimentally using a 5–6- μm CO laser and theoretically. The polarization selection rules for both linearly and circularly polarized light have been investigated. The experimental results are in good agreement with the theoretical predictions. The resonance enhancement of the spontaneous-scattering cross section for an input photon energy near the InSb energy gap has been studied as a function of input photon energy and magnetic field. Good agreement is found between the experimental data and a theoretical treatment which includes both the effects of varying population factors and the k_z dependence of the spin-flip cross section. The linewidth and, where it could be resolved, the line shape of spontaneous-spin-flip Raman scattering was studied experimentally as a function of electron concentration ($1\text{--}3 \times 10^{16} \text{ cm}^{-3}$), temperature (2–50 K), and magnetic field (20–80 kG). Two different geometries were studied. In both geometries, the incident photon propagated normal to the magnetic field \vec{H} . In one geometry the scattered light was collected colinear with the incident light ($\vec{q} \cdot \vec{H} = 0$), while in the other geometry it was collected along \vec{H} at right angles to the incident light ($\vec{q} \cdot \vec{H} \neq 0$). The linewidth in the $\vec{q} \cdot \vec{H} = 0$ geometry was very narrow (0.2–0.4 cm^{-1}) and almost independent of magnetic field. The linewidth in the $\vec{q} \cdot \vec{H} \neq 0$ geometry was strongly dependent on magnetic field. It varied from a maximum of 6.5 cm^{-1} at 21 kG to a minimum of 0.2–0.3 cm^{-1} at 80.5 kG. The linewidth in the $\vec{q} \cdot \vec{H} = 0$ geometry was almost independent of temperature, while the linewidth in the $\vec{q} \cdot \vec{H} \neq 0$ geometry broadened appreciably at higher temperatures. These features of the spin-flip Raman-scattering line shape are shown to be inconsistent with the simplest spin-relaxation theory of the line shape that includes the inhomogeneous broadening due to the nonparabolicity of the InSb conduction band (present in both geometries) and the Doppler shift (in the $\vec{q} \cdot \vec{H} \neq 0$ geometry only). A theory which includes orbital collisions that alter the k_z state of the spin excitation is considered and is found to give results that are in good agreement with the experiment.

I. INTRODUCTION

The spin-flip Raman laser^{1–5} is a promising source of tunable high-power radiation in the infrared region of the spectrum. As a result, the detailed physical properties of spontaneous-spin-flip light scattering in semiconductors have acquired enhanced significance. The near-resonance regime with pump-laser excitation near the 5.2- μm -energy band gap of InSb is of particular interest since it is in this regime that the low-threshold cw operation² of the spin-flip laser has been achieved. This paper gives the results of a detailed experimental and theoretical study of near-resonance spontaneous-spin-flip light scattering from conduction electrons in InSb.⁶ Three main features of the spin-flip Raman scattering have been studied: (i) the polarization selection rules, (ii) the cross-section enhancement for photon energies near the InSb energy band gap, and (iii) the line shape.

Observations of spin-flip light scattering in semiconductors stem from the initial experiments on InSb reported by Slusher *et al.*⁷ Subsequently, conduction-electron spin-flip light scattering has been observed in various III-V,⁸ II-VI,⁹ and lead salt¹⁰ semiconducting materials. By far, the most numerous and detailed studies have involved InSb.^{1–4,6,11} Most previous experiments on InSb have been performed using 10.6- μm CO₂ laser ex-

citation,^{1,3,4,11} in contrast with the present work in which a 5- μm CO laser was used. While various aspects of the spontaneous-spin-flip light scattering in InSb at 10 μm have been reported,^{1,3,4,11} the only characteristic studied in detail was the polarization selection rules.¹¹ Preliminary accounts⁶ of the properties of the scattering for 5- μm excitation have been given by the authors previously.

Theories of inter-Landau-level scattering in semiconductors have evolved from the treatment of Wolff¹² who initially predicted the phenomena and demonstrated the presence of a strong resonance enhancement in the cross section for photon energies near the band-gap energy. This calculation was extended in the low magnetic field limit to include the detailed III-V semiconductor band structure by Yafet.¹³ Subsequently, Wright *et al.*¹⁴ investigated the effects of high magnetic fields on the cross section and the polarization selection rules. Wherrett and Harper¹⁵ and Makarov¹⁶ have considered the effects of electron statistics on the cross section. All of these theories were primarily aimed at properties related to experiments at 10.6 μm . They did not consider matters such as strong resonance enhancement of the cross section and the effects of electron scattering on the line shape which are discussed in detail here.

The polarization selection rules for spin-flip light scattering were investigated using a 5.3- μm

pump beam. Both circular and linear polarizations were studied where appropriate. The results are in excellent agreement with the previously predicted theoretical polarization selection rules.^{13,15,16} This is in contrast to the recently reported results of Patel and Yang¹¹ for the case of 10.6- μm excitation where essentially complete depolarization was found.

The resonance enhancement of the cross section for spontaneous-spin-flip Raman scattering as the incident photon energy approaches the InSb energy gap was studied experimentally by two different techniques. In one measurement the large number of closely spaced laser transitions available from the CO laser in the spectral range from 5.2 to 6.1 μm were used to vary the input photon energy while the magnetic field and, consequently, the InSb energy-level structure was held fixed. After correction for apparatus response and band-edge absorption a variation of over an order of magnitude in the relative cross section was found in this spectral range. An accurate calculation of the cross-section resonance enhancement was carried out using detailed InSb band-edge wave functions and nonparabolic energy-level structure. There is good agreement between this calculation and the experimental measurements over most of the range studied. Some slight deviations for frequencies near the energy gap are outside of the systematic error. These may be related to impurity resonance effects that have been excluded from the present treatment. The second measurement of the resonance enhancement involved varying the magnetic field while holding the input photon energy constant. There are additional physical effects in this measurement that arise from the dependence of the cross section on the electron statistics and orbital quantum numbers. Again, there is qualitatively good agreement between theory and experiment for a variation of almost an order of magnitude in the relative cross section.

Measurements of the spontaneous-spin-flip Raman linewidth and, when possible, line shape were made for various temperatures, electron concentrations, magnetic fields, and scattering geometries. Due to the extremely narrow linewidth in some cases ($< 0.3 \text{ cm}^{-1}$) we were unable to obtain accurate line-shape data for all of the parameter variations measured. Two geometries were investigated: (i) the incident and scattered photons were colinear and propagated normal to the mag-

netic field ($\vec{q} \cdot \vec{H} = 0$ geometry) and (ii) the incident photons again propagated normal to the field but the scattered photons were collected along the field direction ($\vec{q} \cdot \vec{H} \neq 0$ geometry); here, \vec{q} is the scattering wave vector. Striking differences were observed in the behavior of the linewidth in the two geometries as a function of magnetic field and temperature. The linewidth in the $\vec{q} \cdot \vec{H} = 0$ geometry is very narrow ($\lesssim 0.3 \text{ cm}^{-1}$) and almost independent of magnetic field. In contrast, the linewidth in the $\vec{q} \cdot \vec{H} \neq 0$ geometry decreases (for $n \approx 10^{16} \text{ cm}^{-3}$) by over an order of magnitude as the magnetic field is increased from 20 to 80 kG, approaching the narrow linewidth observed in the $\vec{q} \cdot \vec{H} = 0$ geometry. At all magnetic field strengths, there was no observable difference between the linecenter frequencies in the two geometries.

A simple spin-relaxation theory of the linewidth which included inhomogeneous broadening due to energy-band nonparabolicity and the Doppler shift was found to be inconsistent with the experimental data. A phenomenological relaxation-time theory, including orbital collisions, was formulated and is shown to give results in qualitative agreement with experiment. It is shown that the orbital collisions cause a motional narrowing of the inhomogeneously broadened spin-flip line, and can dramatically affect the line shape.

The remainder of this article is organized as follows. Section II gives the theory of spin-flip scattering including a discussion of the cross-section calculation and the theory of the line shape. The experimental apparatus is described in Sec. III. The experimental results and the fit between theory and experiment are outlined in Sec. IV. A brief discussion of the connection between this work and the operation of the spin-flip Raman laser is given in Sec. V. Finally, two appendices give some details on InSb wave functions which are needed for the cross-section calculation and an alternative derivation of the spin-flip line shape.

II. THEORY OF SPONTANEOUS-SPIN-FLIP RAMAN SCATTERING

A. Integrated Cross Section

The calculation of the probability of scattering a photon from an initial state ($\vec{k}_i, \omega_i, \hat{e}_i$) to a final state ($\vec{k}_0, \omega_0, \hat{e}_0$) with an accompanying change in many electron states from an initial state I to a final state F is straightforward and the result^{13,14,16} for the differential cross section is

$$\frac{d^2\sigma}{d\Omega d\omega} = \left(\frac{e^2}{mc^2}\right)^2 \frac{\omega_0}{\omega_i} m^2 \sum_F \sum_I \rho(I) \left| \sum_M \frac{[\hat{e}_0^* \cdot (\vec{v} e^{-i\vec{k}_0 \cdot \vec{r}})_{FM}][(\vec{v} e^{i\vec{k}_i \cdot \vec{r}})_{MI} \cdot \hat{e}_i]}{E_I - E_M + \hbar\omega_i} + \frac{[\hat{e}_i^* \cdot (\vec{v} e^{i\vec{k}_i \cdot \vec{r}})_{FM}][(\vec{v} e^{-i\vec{k}_0 \cdot \vec{r}})_{MI} \cdot \hat{e}_0]}{E_F - E_M - \hbar\omega_i} \right|^2 \hbar \delta(E_F - E_I + \hbar(\omega_0 - \omega_i)) , \quad (2.1)$$

where the E 's are the many-electron energies, M is the intermediate electronic state, the \hat{e} 's are the polarization vectors, the ω 's are the frequencies of the incident and scattered photons, $m\vec{v}$ is the electron momentum operator in the presence of a static magnetic field, and $\rho(I)$ is the statistical probability that the initial electronic state is occupied. This term will be neglected here and the scattering cross section for a single electron will be evaluated. The effects of electron statistics on the integrated cross section will be discussed below.

The single-electron eigenstates in a magnetic field can be expanded¹⁷ as

$$\psi_{b,n,\sigma}(\vec{r}) = \sum_j e^{ik_y y} e^{ik_x z} \int dk_x e^{ik_x [x - (k_y/s)]} \times c_j(b, n, \sigma) \varphi_{n_j}(k_x/\sqrt{s}) u_{j,0}(\vec{r}), \quad (2.2)$$

where b is a band index (c —conduction band, h —heavy-hole band, l —light-hole band, and d —spin-orbit split-off band), n is the Landau-level number, and σ is an index which indicates the effective spin energy levels to which these states belong (α —spin up and β —spin down). The $u_{j,0}(\vec{r})$ are the cell periodic solutions of the zero-field Hamiltonian at the band edge (see Appendix A). The δ -function dependence of the eigenfunctions on k_y and k_x has not been included. The φ_{n_i} are harmonic-oscillator eigenfunctions and $\sqrt{s} = (eH/\hbar c)^{1/2}$ is a parameter with dimensions of (1/length) which characterizes the extent of the wave functions in k_x . The coefficients $c_j(b, n, \sigma)$ are given to lowest order in H (or s) in Appendix A, and n_j is related to n and j by the following convention: $n_1 = n$, $n_2 = n - 1$, $n_3 = n + 1$, $n_4 = n + 1$, $n_5 = n$, $n_6 = n + 1$, $n_7 = n - 1$, and $n_8 = n - 1$.

With the aid of this equation, the matrix elements involved in (2.1) can be evaluated. These are of the form

$$M_{JI} = \delta(k_x - k'_x + q_x) \sum_{i,j} c_j^*(J) c_i(I) \{ \mathcal{P}_{ji} \delta_{n_i, m_j} + [s(n_i + 1)]^{1/2} \delta_{n_i+1, m_j} \hat{e}_- + (s n_i)^{1/2} \delta_{n_i-1, m_j} \hat{e}_+ \}, \quad (2.3)$$

where the \hat{e} 's are unit vectors and $\hat{e}_\pm = (\hat{e}_x \pm i\hat{e}_y)/\sqrt{2}$. The matrix elements of the momentum operator p between the $u_{j,0}(\vec{r})$ are proportional to the inter-band matrix element $P = i(\hbar/m) \langle S | p | X \rangle$. Equation (2.3) has been evaluated in the dipole approximation with the exception that the effects of nonzero photon momentum have been retained in the δ function that represents conservation of momentum in the magnetic field (z) direction. In the present discussion of the integrated cross section this makes little difference; however, it is quite important in the line-shape considerations of Sec. II B

where the fact that the transitions are non- k_x -conserving is shown to be an additional broadening mechanism.

It is at this juncture that the previous treatments of spontaneous-spin-flip Raman scattering have taken different approaches in the evaluation of the cross section. Yafet¹³ and Makarov¹⁶ have expanded the $c_j(b, n, \sigma)$ to first order in the magnetic field and have obtained analytic results for the cross section while Wright *et al.*¹⁴ have computed the $c_j(b, n, \sigma)$ to all orders in H and obtained more precise numerical results. Both of these approaches have been followed in this work. A numerical calculation of the photon energy and the magnetic field dependences of the spin-flip Raman scattering cross section was performed using the Pidgeon and Brown¹⁸ model Hamiltonian to evaluate the InSb band structure. All of the explicit numerical results presented here were obtained by this calculation. In addition, analytic results offer a great deal of physical insight into the spin-flip scattering process and will be briefly discussed. Rather than present the complete result which is quite unwieldy, some of its more interesting features will be pointed out individually and finally a more restricted expression appropriate to the experimental conditions of Sec. IV will be presented. For small magnetic fields [$P(s)^{1/2}/E_g \ll 1$] the mixing of the states due to the magnetic field is negligible and it is sufficient to take the initial- and final-conduction-band states as simply $|S\uparrow\rangle$ and $|S\downarrow\rangle$, respectively. If there were no spin-orbit-mixed valence-band states present, the spin-flip cross section would be identically zero as there is no spin operator in the coupling between the electrons and the photons. It is the availability of valence-band intermediate states such as $|L, \alpha\rangle = (1/\sqrt{6}) |(X - iY)\uparrow + 2Z\downarrow\rangle$, which have a mixed-spin character, that gives rise to the large spin-flip cross section. Clearly, there is an allowed electric dipole transition from both the initial and final electron states to such intermediate states. These mixed-spin states arise because of the spin-orbit interaction which is quite large in InSb ($\Delta \gg E_g$), where Δ is the valence-band spin-orbit splitting energy (~ 0.9 eV) and E_g is the optical-gap energy (0.236 eV at 0 °K). In the absence of spin-orbit coupling the split-off (d) states are degenerate with the light- and heavy-hole states and give rise to a matrix element of opposite phase which just cancels the light- and heavy-hole contributions. The $c_j(b, n, \sigma)$ in Appendix A have been derived under the approximation $\Delta \gg \hbar^2 s/m_c$ and, therefore, do not exhibit this cancellation; however, a similar treatment with the above inequality reversed and also requiring $\Delta < (E_g - \hbar\omega_i)$ readily shows that $d\sigma/d\Omega$ is of order $[\Delta/(E_g - \hbar\omega_i)]^2$. This is important in considering spin-flip Raman scattering

from wide band-gap III-V compounds such as GaAs, where Δ is very much smaller than in InSb.

At larger magnetic fields, where the intermixing of conduction- and valence-band states is stronger, there is a contribution to the cross section which uses a conduction-band state $|c, 1, \beta\rangle$ as the intermediate state. This term has an energy denominator which is resonant for the incident-photon energy equal to the combined resonance frequency ($\Delta n=1, \Delta s=1$). Because of the strong resonance enhancement of the cross-section contributions involving valence-band intermediate states, this term is not significant in the present experiments; however, it can become the dominant contribution to the spin-flip scattering cross section for photon wavelengths of 10 μm or longer.^{19,20}

Finally, consider the terms which are resonant under the present experimental condition of a photon energy near E_g . The dominant physical process in the scattering is the excitation of an electron from the valence band into the upper-conduction-band spin level with the absorption of an incident photon and the relaxation of an electron from the lower-conduction-band spin level into the valence-band state with the emission of the scattered photon. Clearly, the resonance is between the valence-band to upper-spin-level energy and the incident-photon energy. The largest contributions to the cross section occur via light-hole valence-band states of Landau-level number $n=-1$ and via heavy-hole valence-band states. The energies of these states are independent of magnetic field in the present band model and are taken as the zero-energy reference. The expression for the cross section is

$$\frac{d\sigma}{d\Omega} \approx \left(\frac{e^2}{mc^2}\right)^2 \left(\frac{\omega_0}{\omega_i}\right) \left(\frac{mP^2}{3\hbar^2}\right)^2 \left| \left(e_{iz}e_{0z} - \frac{1 - \frac{1}{3}a^2 - \frac{1}{3}b^2 + Aa}{E_{c,0,\beta} - \hbar\omega_i} \right. \right. \\ \left. \left. - \frac{6}{7} e_{iz}e_{0z} \frac{1 - \frac{2}{3}a^2 - \frac{1}{3}b^2 - Aa}{E_{c,0,\beta} - \hbar\omega_i} \right) \right|^2, \quad (2.4)$$

where

$$a = P(s)^{1/2}/E_g, \quad (2.5)$$

$$b = P(s)^{1/2}/(E_g + \Delta), \quad (2.6)$$

$$A = (\hbar^4 s / m^2 P^2)^{1/2}, \quad (2.7)$$

and only the terms closest to resonance have been retained. The intermediate state responsible for the first contribution to the cross section is $|l, -1, \alpha\rangle$ and for the second it is $|h, 1, \beta\rangle$. The terms which arise from light-hole intermediate states ($n \geq 0$) are approximately a factor of 2 further removed from resonance and have therefore not been included above.

It is interesting to note that the $(+, z)$ cross sec-

tion (the first letter indicates the polarization of the incident photon and the second letter the polarization of the scattered photon) is smaller than the $(z, -)$ by a factor of 0.73 (the more detailed numerical computation results in a value of 0.78 for the ratio of the intensities of the two allowed scattering polarizations for a photon energy near the energy gap). In a nonresonant case these intensities are approximately equal for small magnetic fields since the light-hole contributions to the cross section are comparable to the heavy-hole contributions. At high magnetic fields there is another mechanism which gives rise to a difference between the two polarizations. This is the mixing of conduction- and valence-band states which gives rise to the terms in $a, b,$ and A in (2.4). Note that there are no additional polarization selection rules that arise when wave-function mixing is included. This is contrary to the results of Wright *et al.*¹⁴

The expression for the cross section can be written as a product of a factor which is weakly dependent on magnetic field and input photon energy, and an enhancement factor of the form

$$W = \left(\frac{E_g}{E_{c,0,\beta} - \hbar\omega_i} \right)^2 \quad (2.8)$$

for the $(z, -)$ polarization component. The cross section is of the order of $3 \times 10^{-23} \text{ W cm}^2/\text{electron}$. The calculated variation of the cross section for a fixed magnetic field as the photon energy is varied is shown in Fig. 1. Note that the cross section for $(z, -)$ scattering is over two orders of magnitude

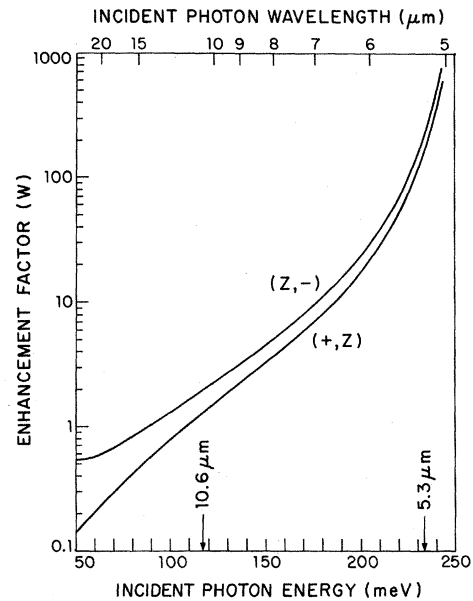


FIG. 1. Variation of the enhancement factor vs input photon energy. Calculated for $H=40 \text{ kG}$; both allowed polarizations $(+, z)$ and $(z, -)$ are shown.

larger at 5.3 μm than at 10.6 μm . The differing behavior of the two polarization components at low photon energies is due to the presence of the conduction-band intermediate state discussed above.

Up to this point the effects of the electron statistics on the integrated cross section have not been evaluated. These effects are incorporated into the theory by integrating the cross-section expression (2.1) to evaluate the total cross section

$$\frac{d\sigma}{d\Omega} = \int_{-\infty}^{\infty} \frac{s}{4\pi^2} |F(k_z)|^2 f_{\alpha}(k_z) [1 - f_{\beta}(k_z)] dk_z, \quad (2.9)$$

where $|F(k_z)|^2$ represents the k_z dependence of the cross section per particle and contains within it the sum over intermediate states of (2.1). For the moment, the k_z dependence of $F(k_z)$ will be ignored and only the direct population effects considered. The effects of this k_z dependence on the total cross section will be considered below. The sum over initial states of (2.1) has been written as the integral over k_z in (2.9) and the probability that the initial electronic state is occupied is given by $f_{\alpha}(k_z)[1 - f_{\beta}(k_z)]$, where $f_{\alpha}(k_z)$ and $f_{\beta}(k_z)$ are the Fermi occupation factors for the spin-up and spin-down levels, respectively. This remaining integral can then be evaluated to give

$$\frac{d\sigma}{d\Omega} \approx |F(0)|^2 (n_{\alpha} - n_{\beta}), \quad (2.10)$$

where the additional approximation $(s/4\pi^2) \int f_{\alpha}(k_z) \times f_{\beta}(k_z) dk_z \approx n_{\beta}$ has been made. This is, of course, exact at zero temperature and is readily shown to be a good approximation in the low-temperature and high magnetic field region that is appropriate to these experiments. Thus, there is a sharp decrease in the spin-flip scattering intensity as the magnetic field is lowered beyond the point where all of the electrons are in the lowest spin state (the quantum limit).

There are two effects that result in the k_z dependence of $F(k_z)$: (i) the electrons at finite k_z are somewhat further removed from resonance than those at $k_z = 0$ and therefore have smaller enhancement factors and (ii) there is a k_z dependence of the scattering matrix elements. Both of these effects are small for most experimental conditions and an approximate evaluation is sufficient. For the resonance contribution, the approximate enhancement factor W (2.8) must be averaged over k_z . If the k_z -dependent part of $E_{c,0,\beta}(k_z)$ is small compared to $[E_{c,0,\beta}(0) - \hbar\omega_i]$, we have

$$W \approx \left(\frac{E_g}{E_{c,0,\beta}(\langle k_z \rangle_{av}) - \hbar\omega_i} \right)^2, \quad (2.11)$$

where

$$\langle k_z \rangle_{av} \equiv \left(\frac{s}{4\pi^2(n_{\alpha} - n_{\beta})} \int dk_z k_z^2 f_{\alpha}(1 - f_{\beta}) \right)^{1/2}, \quad (2.12)$$

which at $T=0$ gives

$$\langle k_z \rangle_{av} = \left[\frac{1}{3} \left(\frac{k_F^3 - k_M^3}{k_F - k_M} \right) \right]^{1/2}. \quad (2.13)$$

Here k_F is the momentum of the electrons in the $|c, 0, \alpha\rangle$ level at the Fermi energy and k_M is the momentum of the electrons in the $|c, 0, \beta\rangle$ level at the Fermi energy. For magnetic fields and densities such that $E_F < E_{c,0,\beta}$, k_M is identically zero. The cross-section calculations discussed above were carried out using the $k_z = 0$ band-edge wave functions of InSb. If the expansion of the eigenfunctions of the magnetic Hamiltonian is carried out to first order in $\hbar^2 k_z^2 / 2m_c E_g$ as well as in the magnetic field, a modification to the dominant terms of (2.7) for the $(z, -)$ polarization selection rule by a multiplicative factor of the form

$$\left(\frac{3s}{3s + 2k_z^2} \right)^2 \quad (2.14)$$

is found. This term can also be estimated by using the value of $\langle k_z \rangle_{av}$. Note that these effects are most significant at low magnetic fields where the Fermi energy is relatively high in the band. At high magnetic fields the electrons are all concentrated near $k_z = 0$ as a result of the high degeneracy of the k_z states and consequently there is little effect due to the k_z variation.

B. Line Shape

In this section a description of the line shape of spin-flip light scattering based on a phenomenological collision model is presented. This description allows insight into many of the physical phenomena which affect the line shape and gives reasonable agreement with the data. A detailed microscopic theory of the spin-flip light scattering line shape has been formulated by Davies.²¹ Davies discusses additional effects which are not included in this simple phenomenological treatment and points out the limits of its applicability.

The experiments reported here were carried out in the quantum limit in which all of the electrons are in the lowest-energy Landau level ($n=0$, spin up) in thermal equilibrium. The Raman process is, therefore, not restricted to exciting electrons at the Fermi surface but can excite an electron with any momentum from the spin-up state to the spin-down state. Because the energy of an electron spin-flip excitation is a function of its momentum (its orbital quantum number k_z) there is a resultant inhomogeneous broadening of the spin-

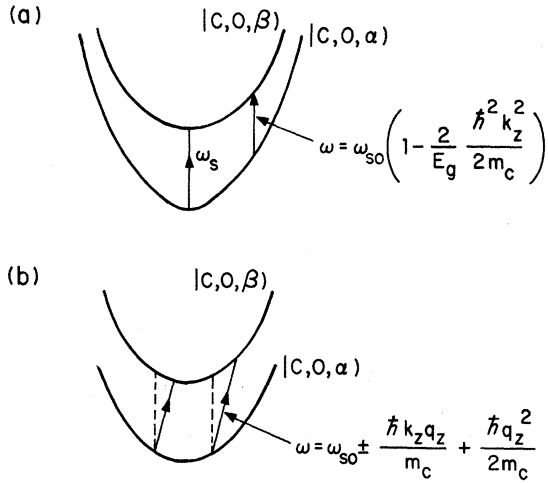


FIG. 2. InSb models used in the line-shape calculations: (a) inhomogeneous nonparabolicity broadening and (b) inhomogeneous Doppler broadening.

flip Raman scattering line shape. The two mechanisms responsible for this orbital dependence of the spin-flip excitation energy are (i) nonparabolicity of the InSb conduction band and (ii) Doppler broadening arising from the momentum imparted to the electrons by the photons. The spin-flip excitation frequency is

$$\omega_s(k_x) = \omega_{s0} + \omega_{NP}(k_x) + \omega_D(k_x),$$

where ω_{s0} is the $k_x = 0$ value of the spin-flip frequency and $\hbar k_x$ is the electronic momentum along the z -directed magnetic field. The nonparabolicity contribution to ω_s is given approximately by

$$\omega_{NP}(k_x) \approx -\omega_{s0} \hbar^2 k_x^2 / m_c E_g, \quad (2.15)$$

where m_c is the electron band-edge effective mass and E_g is the band-gap energy; the contribution of the quantum Doppler shift to the spin-flip frequency is

$$\omega_D(k_x) = -\hbar k_x q_x / m_c + \hbar q_x^2 / 2m_c, \quad (2.16)$$

where q_x is the component of the scattering wave vector $\vec{q} = \vec{k}_i - \vec{k}_f$ along the magnetic field direction. This was noted in conjunction with (2.5) where it was pointed out that conservation of momentum in the z direction requires that $k_{z\beta} = k_{z\alpha} + q_z$, where $k_{z\alpha}$ ($k_{z\beta}$) is the momentum eigenvalue of the initial spin-up (final spin-down) state. These inhomogeneous broadening mechanisms are shown schematically in Fig. 2. Because of the dependence of the Doppler broadening on the direction of the scattering wave vector, and line shape is sensitive to the experimental geometry.

As a result of these orbital dependences of the spin energy, orbital relaxation processes which alter the k_x state of a spin excitation while conserv-

ing the total number of spin excitations can significantly affect the line shape. These effects of orbital collisions on the line shape are treated by a theory first developed in a general form by Davies and Blum.²² This theory was later simplified and applied to the specific case of spin-flip Raman scattering in the quantum limit by Brueck and Blum.⁶ The derivation presented here is based on a density-matrix calculation. An alternate derivation, based on the theory of stochastic processes, is presented in Appendix B. The two derivations, since they involve quite different approaches, present complementary views of the underlying physics.

The theory is characterized by two phenomenological collision times: (i) τ_s , a time that characterizes those processes that either relax the spin excitation or randomly interrupt the phase of the electron spin precession and (ii) τ_p , a time that characterizes the orbital relaxation of this spin excitation. This relaxation corresponds to a collision which alters the k_x state of the spin excitation but does not alter the phase of the spin excitation. As shown by Davies²¹ ionized impurity scattering is an example of a physical mechanism that gives rise to such collisions.

It is perhaps of some value to make contact with the conventions of solid-state maser terminology at this point. The time τ_s corresponds to the T_2 in this notation and is therefore shorter than the spin relaxation time or T_1 . Previous theoretical and experimental evaluations²³ of T_1 indicate a value of 10^{-7} – 10^{-9} sec. There have been numerous experimental investigations of conduction-electron spin resonance in InSb.^{23,24} On the whole these experiments have been carried out in the microwave region of the spectrum and, consequently, were not in the quantum limit even for the comparatively low-density samples that were used. If the linewidths obtained in these measurements are attributed to a simple collisional process, the collision time is $T_2 \sim 10^{-9}$ – 10^{-10} sec. The inhomogeneous broadening mechanisms discussed above were not important in the microwave work where the excitations were confined primarily to the vicinity of the Fermi level. In the calculations that follow, τ_s will be taken as 10^{-10} sec. The calculated line shapes will be displayed as a function of τ_p and this parameter will be adjusted to obtain a good fit with the experimental results. The resultant values of τ_p are comparable to the collision times evaluated from dc mobility considerations as would be expected from the identification of τ_p processes with ionized impurity scattering.

The scattering cross section is conveniently expressed²² in terms of the resonant off-diagonal (in-spin) matrix elements of the one-electron density matrix which satisfies the equation of motion,

$$i\hbar \frac{\partial \rho}{\partial t} = [3c, \rho] + \frac{\partial \rho}{\partial t} \Big|_{\text{coll}} , \quad (2.17)$$

where $\partial \rho / \partial t|_{\text{coll}}$ is a phenomenological collision term. If this equation is linearized, specialized to the quantum limit and Laplace transformed, the result for the off-diagonal component of the density matrix is

$$i\omega \rho_{\alpha\beta}(k_z) = i\omega_s(k_z) \rho_{\alpha\beta}(k_z) + F f_\alpha(k_z) + \frac{\partial \rho_{\alpha\beta}(k_z)}{\partial t} \Big|_{\text{coll}} , \quad (2.18)$$

where $f_\alpha(k_z)$ is the Fermi function for the $|c, 0, \alpha\rangle$ level and F is the spin-flip matrix element for which we make the band-edge approximation for simplicity. The transverse (to the field) momentum components have already been integrated over and the dipole approximation has been made.

To obtain physically consistent results the collision term must, in general, be constructed so that it conserves quantities such as the local electron concentration and the local magnetic field strength, among others. Davies and Blum²² have given a general form for the relaxation term of (2.17) which includes both orbital and spin relaxation processes, and have derived a general cross-section expression for light scattering in semiconductors. For the present purpose, a simplified form of their collision model given by

$$\frac{\partial \rho_{\alpha\beta}}{\partial t} \Big|_{\text{coll}} = -\frac{1}{\tau_s} \rho_{\alpha\beta}(k_z) - \frac{1}{\tau_p} [\rho_{\alpha\beta}(k_z) - f_\alpha(k_z) \rho'_{\alpha\beta}(k_z)] \quad (2.19)$$

can be used; here

$$\rho'_{\alpha\beta}(k_z) = \frac{\int dk_z \rho_{\alpha\beta}(k_z)}{\int f_\alpha(k_z) dk_z} . \quad (2.20)$$

$$\frac{d^2\sigma}{d\Omega d\omega} = |F|^2 \text{Im} \left[\left\langle \frac{1}{\omega - \omega_s(k_z) - i/\tau} \right\rangle \Big/ \left(1 + \frac{i}{\tau_p} \left\langle \frac{1}{\omega - \omega_s(k_z) - i/\tau} \right\rangle \right) \right] , \quad (2.22)$$

where $1/\tau = 1/\tau_s + 1/\tau_p$ and the angular brackets denote an average over k_z , $\langle G(k_z) \rangle \equiv \int G(k_z) f_\alpha(k_z) dk_z / \int f_\alpha(k_z) dk_z$. Note that in the absence of the inhomogeneous broadening mechanisms [$\omega_s(k_z) \equiv \omega_{s0}$] the calculated line shape is independent of τ_p and is just a simple Lorentzian broadened by $1/\tau_s$.

The line shapes calculated from (2.22) in the $\vec{q} \cdot \vec{H} = 0$ geometry with τ_p as a parameter are shown in Fig. 3. The parameters used in the calculation were $H = 35$ kG, $n = 1 \times 10^{16}$ cm⁻³, $T = 0$ K and $\tau_s = 10^{-10}$ sec; the frequency axis is labeled in wave-number deviation from ω_{s0} . In the absence of τ_p collisions, $\tau_p = \infty$, the line shape exhibits a narrow high-relative-intensity structure near ω_{s0} and an asymmetric tail extending towards smaller fre-

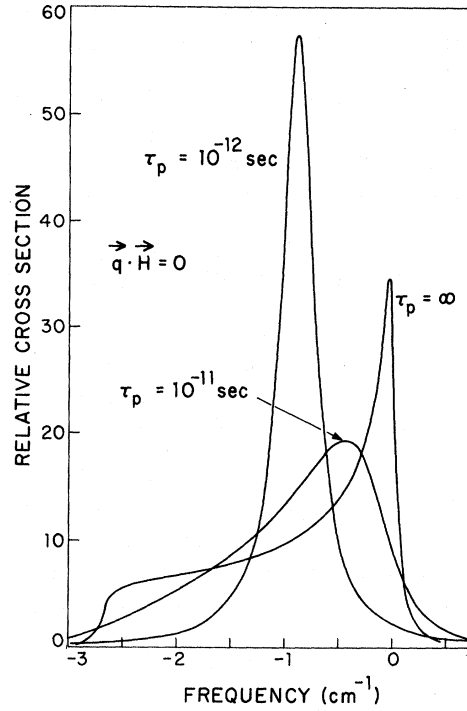


FIG. 3. Effects of orbital collisions on the line shapes in the $\vec{q} \cdot \vec{H} = 0$ geometry. $n = 1 \times 10^{16}$ cm⁻³, $H = 35$ kG, and $\tau_s = 10^{-10}$ sec.

The differential cross section is related to the density matrix by the equation

$$\frac{d^2\sigma}{d\Omega d\omega} = (n_\omega + 1) \text{Im} \int \frac{s}{4\pi^2} dk_z F^* \rho_{\alpha\beta}(k_z) , \quad (2.21)$$

where n_ω is the Bose factor $n_\omega = (e^{\hbar\omega/kT} - 1)^{-1}$. The scattering cross section is readily evaluated,

quency shifts. This long tail results from the spread in spin energies due to the nonparabolicity broadening and the sharp structure near ω_{s0} results from the $\epsilon^{-1/2}$ divergence in the density of states of the spin excitation at the band edge. The singularity is rounded over here because of the τ_s collisional broadening. Davies²¹ and Auyang and Wolff²⁵ have considered the effects of a more accurate treatment of the density of states on the spin-flip line shape. For this case of $\tau_p = \infty$, Eq. (2.22) takes the simple form

$$\frac{d^2\sigma}{d\Omega d\omega} = |F|^2 \text{Im} \left\langle \frac{1}{\omega - \omega_s(k_z) - i/\tau_s} \right\rangle \quad (2.23)$$

and the line shape is a simple Lorentzian broad-

ened by the inhomogeneous spread in spin energies. As τ_p is decreased below τ_s , there is first a broadening and smearing out of the sharp structure near $k_x=0$, as would be expected from the addition of more collisions. However, as τ_p is decreased still further, the line shape narrows and becomes quite symmetrical. Further decreases in τ_p continue this process. The peak of the curve is shifted towards the center of the inhomogeneous frequency distribution and the linewidth is a strong function of τ_p .

These striking effects on the line shape can be understood in terms of the concepts of motional narrowing,²⁶ well known in the field of nuclear magnetic resonance. At each τ_p collision, the frequency of the spin excitation is randomly increased or decreased as a result of the random variation in k_x . If these collisions occur sufficiently frequently that electrons which are in phase at $t=0$ and in different k_x states are scattered before they can become significantly out of phase, i. e., if

$$\Delta\omega_s\tau_p \equiv |(\omega_s(k_p) - \omega_{s0})| \tau_p \lesssim 1, \quad (2.24)$$

there will be significant effects on the line shape. This is just the usual condition for the presence of motional-narrowing effects. The apparent broadening before the onset of this narrowing in Fig. 3 is just the result of the complicated density of states in the absence of τ_p collisions. If $\Delta\omega_s$ is taken as the width of the line in the absence of τ_p collisions, there is a consistent narrowing of the linewidth as τ_p is decreased. The line shape in the limit of extreme motional narrowing, where the initial density-of-states effects are almost completely obliterated, can be derived on the basis of a simple heuristic argument which is closely related to the derivation of (2.21) presented in Appendix B. Consider a spin excitation initiated at $t=0$ undergoing rapid τ_p collisions. After many such collisions, the average phase change for the spin excitation is

$$\Delta\varphi_{av} = [\langle\omega_s(k_x)\rangle] t \quad (2.25)$$

and, correspondingly, the frequency of maximum scattering intensity will be

$$\omega = \langle\omega_s(k_x)\rangle = \omega_{s0} \left(1 - \frac{\hbar^2 k_x^2}{3m_c E_g}\right). \quad (2.26)$$

The linewidth is proportional to the variance of the phase change $\Delta\varphi$;

$$\sigma^2(\Delta\varphi) \equiv E(\Delta\varphi^2) - [E(\Delta\varphi)]^2, \quad (2.27)$$

where the E denotes the expectation value over an ensemble of spin excitations. The phase is accumulated in a series of discrete steps, between collisions, of magnitude $\Delta\varphi_i = \omega(k_{xi})\tau_p$, where the duration of each step has been set at τ_p . The distribution of collision times for each step could be

retained, but only at the price of more complicated mathematics (see Appendix B). The number of discrete steps is $n = t/\tau_p$. Then,

$$\begin{aligned} \sigma^2(\Delta\varphi) &= E\left(\sum_i \{\Delta\varphi_i - [E(\Delta\varphi_i)]\}^2\right) \\ &= \frac{t}{\tau_p} E\{\Delta\varphi_i^2 - [E(\Delta\varphi_i)]^2\}, \end{aligned} \quad (2.28)$$

where the relationship between the variance of a sum of identical independent random variables and the variance of one such variable has been used. The final result for the linewidth is

$$\Delta\omega = \sigma^2/t = \tau_p [\langle\omega_s^2(k_x)\rangle - \langle\omega_s(k_x)\rangle^2], \quad (2.29)$$

which is proportional to τ_p . The same result is obtained from (2.21) in the limit $\tau_p \ll \tau_s$, $\Delta\omega_s\tau_p \ll 1$, and $(\omega - \omega_{s0})\tau_p \ll 1$.

Figure 4 shows the results of applying (2.21) to the calculation of the line shape in the $\vec{q} \cdot \vec{H} \neq 0$ geometry. The effects are qualitatively the same as in the $\vec{q} \cdot \vec{H} = 0$ geometry. The much larger extent of the inhomogeneous broadening in this case is due to the additional Doppler broadening. Since the Doppler broadening is linear in k_x , [(2.16)] the resultant line shape extends to both sides of ω_{s0} . The peak of the line shape is shifted to larger energies due to an interplay between the two inhomogeneous broadening mechanisms. At smaller frequency shifts the two mechanisms add while at

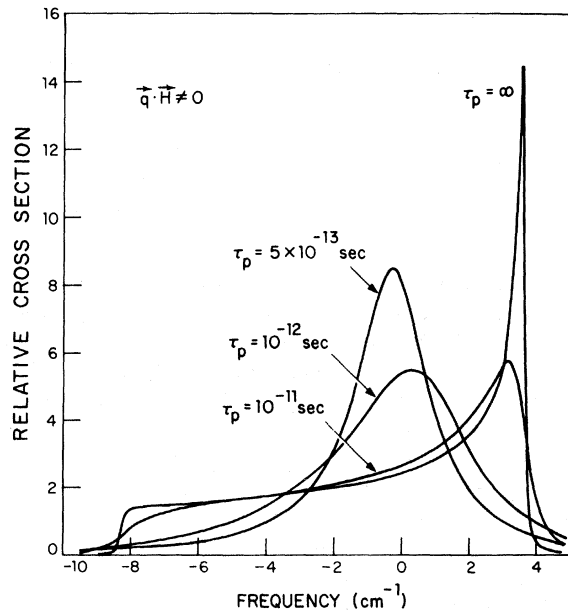


FIG. 4. Effects of orbital collisions on the line shapes in the $\vec{q} \cdot \vec{H} \neq 0$ geometry. $n = 1 \times 10^{16} \text{ cm}^{-3}$, $H = 35 \text{ kG}$, and $\tau_s = 10^{-10} \text{ sec}$.

larger shifts they subtract leading to a slower variation with k_x and hence a larger density of states and a larger contribution to the cross section. The increased extent of the inhomogeneous broadening in the case results in broader lines for the same τ_p , as is predicted by (2.29). In the extreme motional-narrowing limit, the frequencies of the line-shape peaks in the two geometries are separated only by $\hbar^2 q_x^2 / 2m_c$ rather than the much larger separation of the inhomogeneously broadened line shapes.

III. EXPERIMENTAL APPARATUS

The CO laser used in these experiments was a liquid-nitrogen-cooled flowing-gas system similar to that first described by Osgood *et al.*²⁷ The output coupler consisted of a germanium substrate with a 10-m radius of curvature and a dielectric coating with $85 \pm 3\%$ reflectivity from 5 to 6 μm . A gold-coated 5.2- μm grating blazed at 15° was used as the second laser mirror to allow the laser to be tuned to any of about 60 lines between 5.2 and 6 μm . Typical multimode output powers under these conditions were about 3–4 W on any of a number of strong lines around 5.3 μm . With a reduction in output power to about 1 W the laser could be constrained to operate in a TEM_{00} mode by means of a variable aperture located within the optical cavity.

Two different superconducting magnets were used. The majority of the data was taken using a 50-kG horizontal-bore (1-in. diameter) magnet with straight-through optical access ($f/3$). The bore of the magnet was in the vacuum section of the Dewar and the samples were conduction cooled. The second magnet, which was used to obtain some of the line-shape data reported in Sec. IV, was a 100-kG magnet mounted vertically in a variable-temperature Dewar. Optical access was through a $f/4$ bottom window. The experiments in this magnet were predominantly carried out with the sample immersed in superfluid helium ($T \sim 1.6$ K).

The scattered light was analyzed with a $\frac{3}{4}$ -m grating spectrometer (maximum resolution ≈ 0.1 cm^{-1}) and a Cu:Ge detector ($3 \times 3 \times 3$ mm) operating at liquid-helium temperature was used. In order to reduce the background radiation incident on the detector, cooled apertures ($f/4$) were used and in addition a thin (0.003-in.) sapphire window mounted in front of the detector at liquid-helium temperature was used to eliminate most of the 300-K blackbody radiation incident on the detector. The electrical circuit used is described by Quist²⁸ and includes a metal-film load resistor (2 M Ω) mounted on the helium block and a low-noise field-effect transistor, operated as a source follower, mounted on the nitrogen shield. With this arrangement the noise equivalent power at 500 K was measured to be 10^{-11} W in a 1-Hz band width.

The polarizations of the incident CO-laser beam and the Raman-scattered beam were controlled by using sapphire $\frac{1}{2}$ - and $\frac{1}{4}$ -wave plates. A gold-wire-grid polarizer of polarization ratio 1:200 was used as the polarization analyzer. All of the data presented below have been corrected for the spectrometer wavelength and polarization response.

The samples used were commercially obtained, tellurium-doped *n*-type InSb with liquid-nitrogen temperature carrier concentrations of 0.96–3.3 $\times 10^{18}$ cm^{-3} and mobilities of 145 000–93 000 $\text{cm}^2/\text{V sec}$.

IV. EXPERIMENTAL RESULTS

A. Spin-Flip Energy

Figure 5 shows the tuning characteristics of spin-flip Raman scattering as a function of magnetic field strength in the range 20–80 kG. The data in the $\vec{q} \cdot \vec{H} = 0$ geometry, where measured, was used in determining the frequency shift as the narrower linewidth resulted in higher accuracy. The solid curve in the figure is the $k_x = 0$ electron spin-flip energy calculated by Johnson and Dickey.²⁹ This calculation involved a fit to intraband data on the electron *g* value obtained by electron-spin-resonance and combination-resonance experiments. It is used here rather than the calculation of Pidgeon, Mitchell, and Brown,³⁰ which is based on interband measurements, as several authors have pointed out a discrepancy between the intraband and interband calculations.^{29,31,32}

The agreement between theory and experiment is within experimental error. The dominant source of error, as indicated in the figure, is the uncertainty in the magnetic field calibration. As pointed

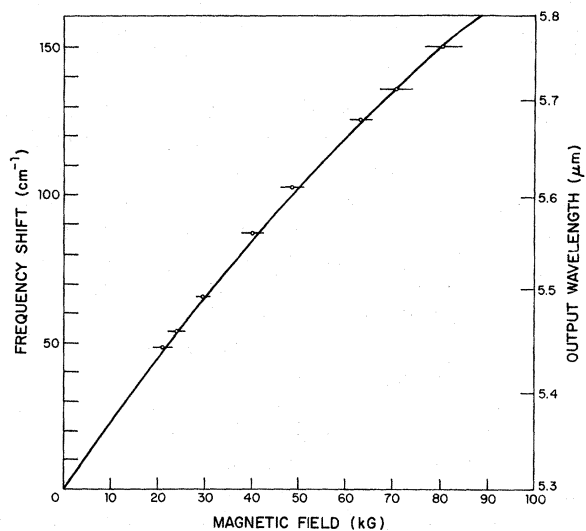


FIG. 5. Frequency shift from incident laser line vs magnetic field strength.

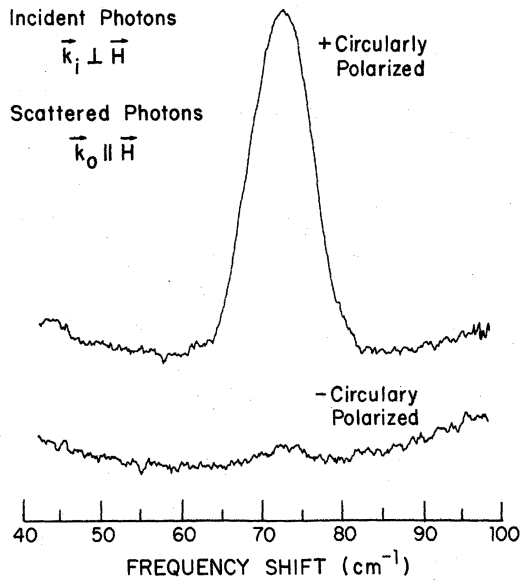


FIG. 6. Polarization of spin-flip Raman scattering. The incident photons are propagating normal to \vec{H} and polarized along $\vec{H}(k_{ix}, E_{iz})$. The scattered light is propagating along $\vec{H}(k_{ox})$ and is circularly polarized. $H = 35$ kG and $T \sim 30^\circ$ K.

out in Sec. II B, due to the effects of orbital collisions on the line shape, the peak of the spin-flip scattering line shape does not necessarily correspond to the bottom of the band value of the spin-down to spin-up energy difference. Except for the data obtained at the lowest magnetic fields this effect should produce a negligible alteration in the theory of less than 1%.

B. Polarization

In Sec. II A, the polarization selection rules for spin-flip Raman scattering were shown to be $(z, -)$ and $(+, z)$, where \pm refer to circular polarizations of photons propagating along the magnetic field and z refers to a photon polarized along the magnetic field direction and, therefore, propagating at right angles to the field. The first (second) term in each selection rule refers to the polarization of the incident (scattered) photon. These selection rules do *not* imply that one of the photons must be propagating along the field, rather they imply only that one photon must be polarized along the field and one polarized at right angles to the field. For example, (z, \hat{x}) scattering where both photons are propagating normal to the magnetic field is included in the $(z, -)$ scattering polarization selection rule. Within the model of the InSb band structure used in Sec. II, these selection rules are independent of crystal orientation; some of the effects of crystal orientation on the polarization selection rules resulting from more detailed models of the InSb band structure have been estimated to shown to be

small.¹⁹

A sample of n -type InSb of electron concentration $1 \times 10^{16} \text{ cm}^{-3}$ was mounted in the 50-kG magnet with an array of small gold mirrors so that the incident laser could be propagated both along the magnetic field and normal to the magnetic field and the scattered light could be collected from all three orthogonal spatial directions. The data was taken at magnetic fields of 35 and 40 kG and the incident-photon energy was 232.0 meV. The scattered light was collected from a solid angle inside the sample of approximately 0.001 sr (this corresponds to an angular spread of $\sim 1^\circ$) in order to avoid any depolarization effects due to too large a collection angle.

Figure 6 shows typical polarization data obtained with the incident photons propagating normal to \vec{H} and the scattered photons propagating along \vec{H} . The sapphire $\frac{1}{4}$ -wave plate in conjunction with a linear polarizer was used to analyze the circular-polarization components. Because the optic axis of the sapphire plate was only known to within a $\frac{1}{2}\pi$ rotation, an assignment of the two polarizations to right and left circular polarization cannot be made. The polarization measurements are summarized in Table I. As a result of the variation in the collection optics for different directions of propagation of the scattered light, the results within each set of data delineated by the double lines are normalized to the maximum theoretical value of the allowed polarization within the set and no comparison can be made between these data sets. The agreement between theory and experiment is quite good. The slight depolarization measured can be attributed, at least partially, to the effects of the collection optics. Patel and Yang¹¹ have measured the polarization selection rules for spin-flip Raman scattering under 10.6- μm excitation and have found violations of these selection rules. The discrepancy between these two measurements has yet to be resolved.

C. Resonance Enhancement

The resonance enhancement of the spin-flip Raman-scattering cross section as the pump-photon energy approached the band-gap energy was studied by two different techniques. In one measurement, the magnetic field and therefore the InSb energy levels were held fixed while the incident-photon energy was varied. In the second measurement, the incident-photon energy was held fixed while the magnetic field was varied. In addition to the resonance variation in this case, the effects due to the population factors and k_x dependence of the cross section which were discussed in Sec. II A are also important.

Figure 7 shows the results of the first measurement at a fixed magnetic field of 40 kG. The CO-

TABLE I. Polarization selection rules for spin-flip Raman scattering—comparison of theory and experiment. The experimental values within each set of double lines are normalized to the maximum theoretical value within that set. $n=1 \times 10^{16} \text{ cm}^{-3}$, $H=35 \text{ kG}$, and $T \sim 30 \text{ }^\circ\text{K}$.

SCATTERED PHOTONS		INCIDENT PHOTONS					
		$\vec{k}_i \perp \vec{H}$				$\vec{k}_i \parallel \vec{H}$	
		$\vec{E}_i \parallel \vec{H}$		$\vec{E}_i \perp \vec{H}$		$\vec{E}_i = \frac{1}{\sqrt{2}}(\vec{E}_{i+} + \vec{E}_{i-})$	
		Experiment	Theory	Experiment	Theory	Experiment	Theory
$\vec{k}_o \perp \vec{H}$	$\vec{E}_o \parallel \vec{H}$	0.06	0.0	0.69	0.78	0.78	0.78
	$\vec{E}_o \perp \vec{H}$	1.0	1.0	0.12	0.0	0.07	0.0
$\vec{k}_o \parallel \vec{H}$	\vec{E}_{o-}	1.0	1.0	0.04	0.0	<0.1	0.0
	\vec{E}_{o+}	0.02	0.0	0.04	0.0	<0.1	0.0

laser photon energy was changed by tilting the cavity grating. This alteration of the laser alignment resulted in slight changes in the directional characteristics of the laser beam and in the laser mode pattern; the optical alignment was, therefore, readjusted for each measurement. These alignment variations were the dominant source of error, about 10–15%, in measuring the magnitude of the received signal. The experiment was carried out in the $(z, -)$ polarization geometry but only the x component of the scattered light was collected so that the data could be corrected for the spectrometer polarization dependence. Since these measurements were carried out very close to the InSb band edge, absorption effects were significant. Accordingly, the sample absorption was measured¹⁹ and the multiplicative correction

$$[(1 - e^{-\alpha_i l})e^{-\alpha_i d}e^{-\alpha_0 x}/\alpha_i]^{-1}, \quad (4.1)$$

where α_i is the absorption coefficient for the incident light and α_0 the absorption coefficient for the scattered light, was applied to the data. In Eq. (4.1), l is the length of the spectrometer slit image on the sample ($\approx 5 \text{ mm}$), d is the distance from the bottom of the sample to the bottom of this image ($\approx 0.5 \text{ mm}$), and x is the distance from the laser beam to the sample face ($\approx 1 \text{ mm}$). The corrected data is shown in Fig. 8 along with the theoretical resonance curve based on the results of Sec. II A. The band parameters of Pidgeon and Brown¹⁸ were used in the calculation; reasonable variations in these parameters would have only a small effect on the computed resonance curve. Thus, only one adjustable parameter—an overall multiplicative factor—was used in the fit between

theory and experiment.

There is qualitatively good agreement between theory and experiment for a variation of over an order of magnitude in the relative cross section. There is some structure in the experimental results

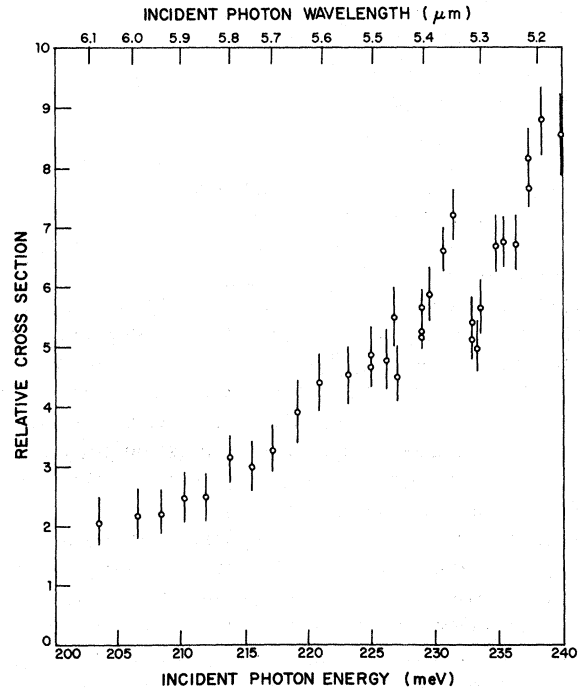


FIG. 7. Relative cross section vs input photon energy uncorrected for sample absorption. $H=40 \text{ kG}$ and $T \sim 30 \text{ }^\circ\text{K}$. The incident photons are propagating normal to \vec{H} and polarized along \vec{H} . The x -linear polarization component of the light scattered along \vec{H} is collected.

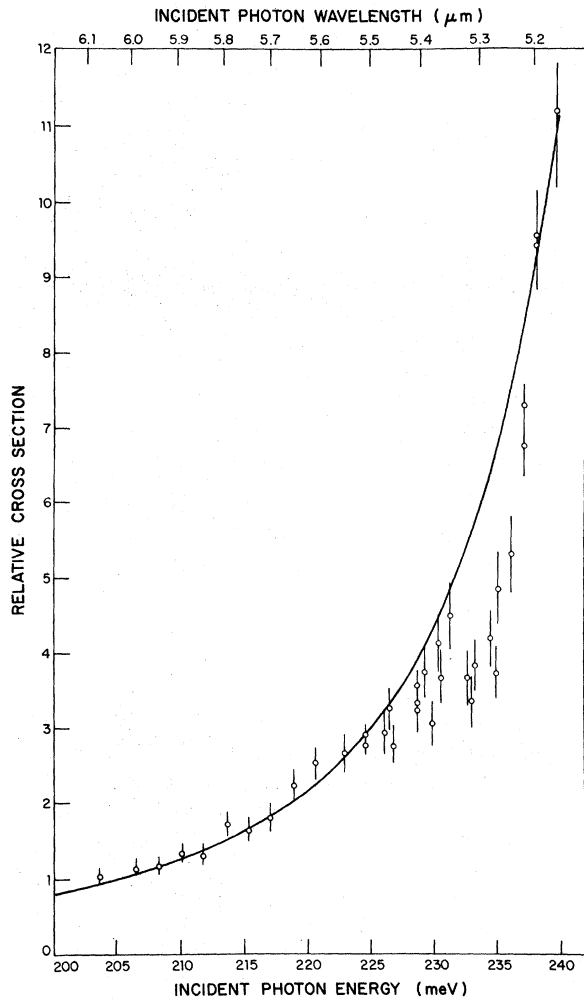


FIG. 8. Resonance enhancement of spontaneous spin-flip Raman scattering as the input photon energy is varied. $n = 1 \times 10^{16} \text{ cm}^{-3}$, $H = 40 \text{ kG}$, and $T \sim 30 \text{ }^\circ\text{K}$.

for input-photon energies around 235 meV that is not predicted by the theory. This might arise from Raman processes that proceed via an impurity level as the intermediate state. There is a Zn acceptor level at about 229 meV at $\vec{H} = 0$. This acceptor level has an energy of about 236 meV at the magnetic field (40 kG) at which this measurement was made.³³ These levels must be included in the sum over intermediate states of (2.1); because of possible interference effects, the result of including these states is not immediately evident. Further study is necessary to resolve this point.

The second experimental measurement of the resonance enhancement was carried out in the 100-kG magnet with a sample temperature of about 5 K. The experimental geometry was the same as that described above. Again the x -polarization component of the scattered light was collected. The laser photon energy was maintained at 229.78

meV. The results, corrected for spectrometer response, as shown in Fig. 9. As the sample absorption is small and almost invariant at both the incident and scattered frequencies, no correction for sample absorption was made. The drop at high magnetic fields is due to decreased resonance enhancement while that at low fields is due to changing population factors and the k_z dependence of the cross section. Again there is only one adjustable parameter in the comparison between theory and experiment: an overall scaling factor. This was selected by forcing the theory and experiment to fit near the peak of the curves, i. e., around 30 kG. There is qualitative agreement between theory and experiment over a range of approximately five in the relative cross section. The fit at the low magnetic fields is reasonable, considering all of the approximations made in treating the k_z dependence of the cross section in Sec. II A. There is a slight deviation at the higher magnetic fields that is outside of experimental error. Possibly this is related to the discrepancy between theory and experiment that was noted in the data involving variation of the input-photon energy.

D. Line Shape

Experimental determinations of the line shape of spin-flip light scattering were carried out in the two geometries discussed in Sec. I; the ($\vec{q} \cdot \vec{H} = 0$) collinear geometry with both the incident and scattered photons propagating across the magnetic field and the ($\vec{q} \cdot \vec{H} \neq 0$) geometry with $\vec{k}_i \perp \vec{H}$ and $\vec{k}_s \parallel \vec{H}$.

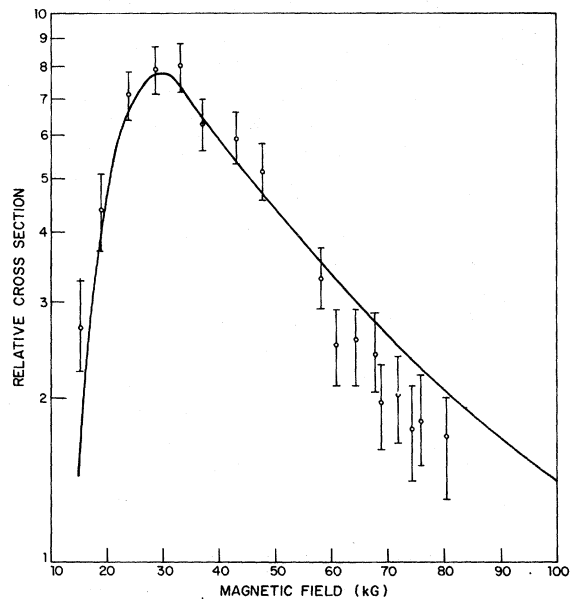


FIG. 9. Comparison of theory and experiment for the variation of the relative cross section vs magnetic field strength. $n = 1 \times 10^{16} \text{ cm}^{-3}$, $T \sim 5 \text{ }^\circ\text{K}$, $\hbar\omega_i = 230 \text{ meV}$.

In the following figures, the resolution indicated is the full width at half-height of the spectrometer response to excitation by a suitably attenuated laser source. The full width at half-height of the spontaneous scattering will be referred to as the linewidth. In calculating linewidths from the data the relationship $\Gamma_C^2 = \Gamma_O^2 - \Gamma_R^2$ between the computed linewidth Γ_C , the observed linewidth Γ_O , and the spectrometer resolution Γ_R , has been assumed. The actual linewidths are probably smaller than Γ_C .

All of the data presented in this section were taken with an incident-photon energy of 233.46 meV (5.30 μm). Several spectral traces were also taken with an incident-photon energy of 230.0 meV (5.38 μm). There was no observable difference between the line shapes at the two pump frequencies.

Figure 10 shows the line-shape data taken with a sample of concentration $1 \times 10^{16} \text{ cm}^{-3}$ at a magnetic field of 24 kG and a temperature of 2 K. Spectra are shown for the two geometries $\vec{q} \cdot \vec{H} \neq 0$ (top) and $\vec{q} \cdot \vec{H} = 0$ (bottom). Note the difference in the frequency scales. The linewidth in the $\vec{q} \cdot \vec{H} \neq 0$ geometry (4.7 cm^{-1}) is over an order of magnitude larger than the linewidth in $\vec{q} \cdot \vec{H} = 0$ geometry (0.3 cm^{-1}). The peak positions are identical to within the accuracy of the measurement ($\lesssim 1 \text{ cm}^{-1}$).

The linewidth data as a function of magnetic field are summarized in Fig. 11. The salient features are: (i) the linewidth in the $\vec{q} \cdot \vec{H} = 0$ geometry is quite

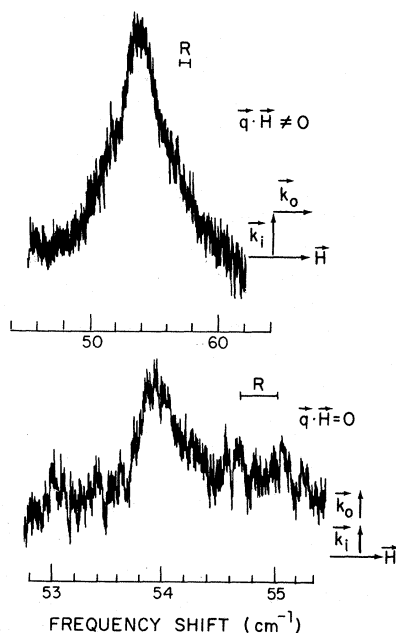


FIG. 10. Line shape of spin-flip Raman scattering ($n = 1 \times 10^{16} \text{ cm}^{-3}$, $H = 24 \text{ kG}$, and $T = 2 \text{ K}$). Spectra are shown for the two geometries $\vec{q} \cdot \vec{H} \neq 0$ (top) and $\vec{q} \cdot \vec{H} = 0$ (bottom).

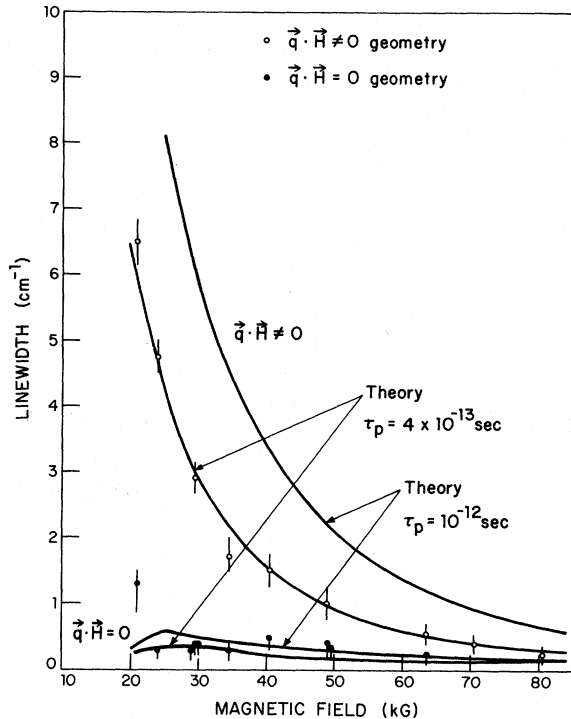


FIG. 11. Comparison of the experimentally observed linewidth with the line-shape theory including orbital collisions. $n = 1 \times 10^{16} \text{ cm}^{-3}$ and $\tau_s = 10^{-10} \text{ sec}$.

narrow (0.2–0.4 cm^{-1}) and almost field independent to within the accuracy of the experiment and (ii) the linewidth in the $\vec{q} \cdot \vec{H} \neq 0$ geometry exhibits a dramatic variation with magnetic field from a maximum of 6.5 cm^{-1} at 21 kG to less than 0.3 cm^{-1} at 80.5 kG.

The solid curves of Fig. 11 show the linewidth as a function of magnetic field predicted by (2.21) with τ_p as a parameter. As noted in Sec. II B, a τ_s of 10^{-10} sec was used in this calculation. A good fit between theory and experiment is obtained for $\tau_p = 4 \times 10^{-13} \text{ sec}$ which is on the order of the electron collision time calculated from the dc mobility ($\mu = 145000 \text{ cm}^2/\text{V sec}$; collision time $\tau \sim 10^{-12} \text{ sec}$). In the $\vec{q} \cdot \vec{H} = 0$ geometry, the experiments are in the motional-narrowed limit for a τ_p of $4 \times 10^{-13} \text{ sec}$ [$(\Delta\omega_s)\tau_p \sim 0.2$ at 35 kG] and the linewidth is given by the approximate analytic result of Eq. (2.28) with the exception that an additional linewidth contribution due to the collisional τ_s broadening must be added. The net effect is to give a nearly field-independent linewidth which is dominated at the higher magnetic fields by the τ_s contribution and which increases as the magnetic field is decreased because of the increasing spread in the inhomogeneous broadening. In the quantum limit, $\epsilon_F \propto 1/H^2$ and consequently $\Delta\omega_s \propto 1/H$ and the "inhomogeneous" linewidth contribution of

(2.28) is proportional to $1/H^2$. Similar effects occur in the $\vec{q} \cdot \vec{H} \neq 0$ geometry but now the "inhomogeneous" linewidth contribution dominates over the collisional term. Again, the inhomogeneous spread in frequencies is proportional to $1/H$ and the linewidth is proportional to $1/H^2$. Further effects occur in this geometry because the line shape is in a transitional region where the motional-narrowing limit has not fully been reached, $[(\omega_s(k_F) - \omega_s(-k_F))\tau_p] \sim 1.2$ at 35 kG. Figure 12 shows the difference in the frequencies of the spontaneous line-shape peaks in the two geometries as a function of magnetic field. The solid curves show the calculated shifts with τ_p as a parameter. Again good agreement is obtained for a τ_p of 4×10^{-13} sec while the theory in the absence of orbital collisions ($\tau_p = \infty$) is totally inadequate.

Figure 13 shows linewidth data taken at a higher temperature of ~ 50 K. The linewidths in the $\vec{q} \cdot \vec{H} = 0$ geometry are approximately magnetic field independent and the widths are comparable to those measured at low temperature; the linewidths in the $\vec{q} \cdot \vec{H} \neq 0$ geometry again show a strong magnetic field dependence but are now considerably larger than at 2 K. For example, at 25 kG the linewidth at 2 K in the $\vec{q} \cdot \vec{H} \neq 0$ geometry is 4.7 cm^{-1} while at 50 K it is 9 cm^{-1} . In the $\vec{q} \cdot \vec{H} \neq 0$ geometry the linewidth is now outside of the motional-narrowed limit and the full expression (2.21) must be used to evaluate the linewidth.

Only limited data were obtained on the variation

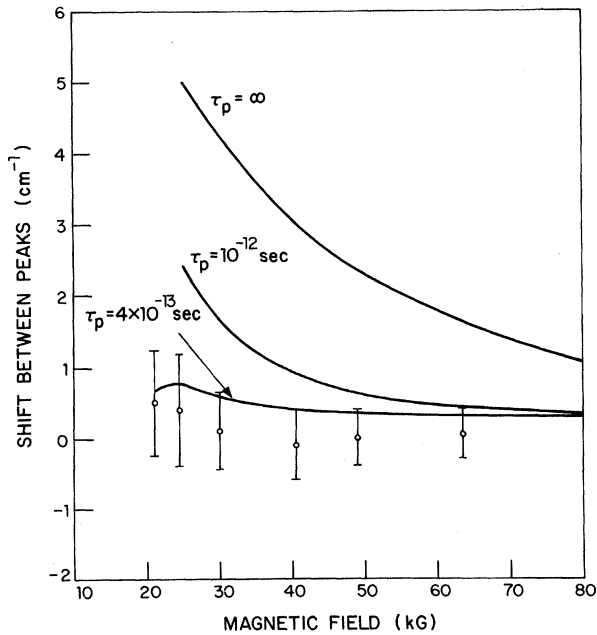


FIG. 12. Comparison of theory and experiment for the peak separation of the line shapes in the two geometries with τ_p as a parameter. $n = 1 \times 10^{16} \text{ cm}^{-3}$ and $\tau_s = 10^{-10} \text{ sec}$.

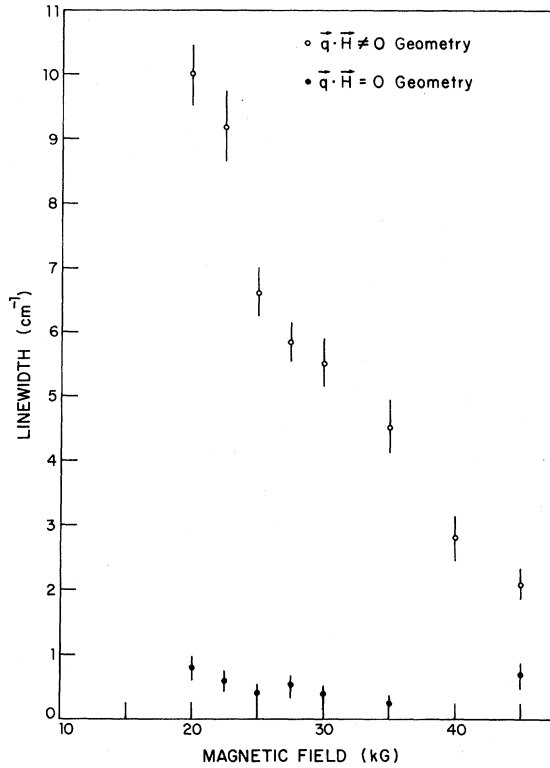


FIG. 13. Linewidth of spontaneous-spin-flip Raman scattering vs magnetic field strength for the two geometries $\vec{q} \cdot \vec{H} = 0$ and $\vec{q} \cdot \vec{H} \neq 0$. $n = 1 \times 10^{16} \text{ cm}^{-3}$ and $T \approx 50 \text{ K}$.

of these linewidths with electron concentration and a detailed fit was not attempted. Figure 14 shows the linewidth in the $\vec{q} \cdot \vec{H} \neq 0$ geometry for samples of concentration $3.3 \times 10^{16} \text{ cm}^{-3}$ (top) and $1 \times 10^{16} \text{ cm}^{-3}$ (bottom) ($H = 35 \text{ kG}$ and $T \sim 20 \text{ K}$). For an electron concentration of 3.3×10^{16} , the Fermi energy is well above the energy of the upper spin state and consequently the inhomogeneous line shape for $\tau_p = \infty$ is a double-peaked structure with a minimum corresponding to the absence of scattering from the electrons near $k_x = 0$. The dip in the experimental curve of Fig. 13 is due to a water-vapor absorption line and did not repeat upon successive measurements of the line shape at slightly different magnetic fields. For a τ_p of 4×10^{-13} sec, the theoretical line shape has a single peak and a linewidth of 17.5 cm^{-1} ; much wider than the observed linewidth of 3.5 cm^{-1} . Decreasing τ_p to 1×10^{-13} sec results in a theoretical linewidth of 3.8 cm^{-1} in good agreement with the experimental results. This seems to indicate that τ_p is inversely related to the electron density as would be expected for ionized impurity scattering. The fit between theory and experiment for the shift between the peak positions of the line shape in the 1.2×10^{16} - and the 3.3×10^{16} - cm^{-3} samples is not as satisfactory. The

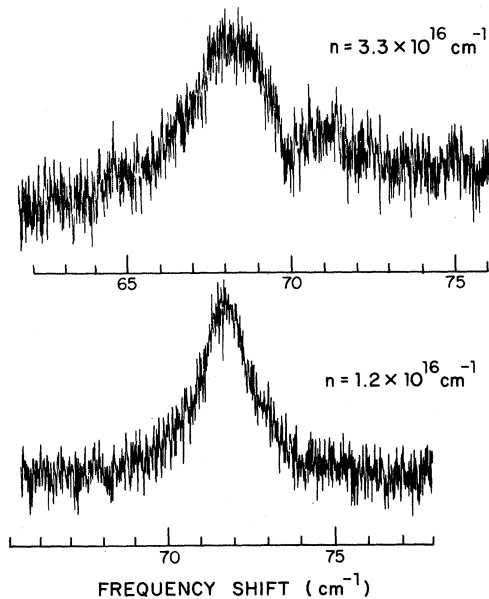


FIG. 14. Line shape of spontaneous-spin-flip Raman scattering. $\vec{q} \cdot \vec{H} \neq 0$ geometry, $H=35$ kG and $T \approx 20$ °K. The top spectrum is for $n=3 \times 10^{16}$ cm $^{-3}$ and the bottom one for $n=1 \times 10^{16}$ cm $^{-3}$.

theoretical prediction is 6.5 cm $^{-1}$; considerably larger than the observed shift of 3.6 cm $^{-1}$.

V. DISCUSSION

The results of the previous sections can be used to gain insight into the operation of the spin-flip Raman laser. Some of the more evident connections such as calculations of threshold powers and fine-tuning characteristics for the 5- μ m cw spin-flip laser have been discussed in detail elsewhere^{2,19} and will not be repeated here. From the line-shape and polarization results of Sec. IV, it is clear that the optimal cavity geometry for operation of the spin-flip laser is in a $\vec{q} \cdot \vec{H} = 0$ collinear geometry. A collinear geometry is of course desirable since it maximizes the gain length for the stimulated scattering. The only collinear geometry that is allowed by the polarization selection rules is the $\vec{q} \cdot \vec{H} = 0$ geometry with both laser beams propagating at right angles to the magnetic field. The linewidth results also indicate that this is a favorable geometry since the linewidth is much narrower than in the $\vec{q} \cdot \vec{H} \neq 0$ geometry. For 10.6 μ m operation of the spin-flip laser, the contribution of inhomogeneous Doppler broadening to the spin-flip linewidth is a factor of 2 smaller than at 5 μ m and this will result in a smaller but still significant difference in the linewidth in the two geometries for magnetic fields less than about 60 kG.

Some interesting features of the total tuning

range of the stimulated scattering for a fixed input power density as a function of magnetic field and input photon energy can be deduced from the results on the resonance enhancement and linewidth discussed above. A larger overall tuning range for the (first-Stokes) stimulated-spin-flip laser can be obtained by varying the input photon energy rather than varying the magnetic field. Quasicontinuous tuning could be obtained by changing CO laser transitions and tuning between the transitions (which are separated by 1–4 cm $^{-1}$) with small magnetic field variations. The reason for this greater tunability is evident upon examination of the energy denominator that enters into the resonance enhancement factor W of (2.8). Decreasing $\hbar\omega_i$ by an amount $\hbar\Delta\omega_i$ results in the resonant denominator being shifted further out of resonance by just that amount; however, if the same tuning is accomplished by varying the magnetic field, $\Delta H = \Delta\omega_i(m'_c c/e)$, the resultant increase in the resonance denominator is $\frac{1}{2}\hbar e\Delta H(1/m_c + 1/m'_c) \approx 3\hbar\Delta\omega_i$ because the resonance is between the input photon energy and the energy of the upper level.

ACKNOWLEDGMENT

We wish to acknowledge helpful discussions with A. L. McWhorter, R. W. Davies, Y. C. Auyang, and P. A. Wolff, and the expert technical assistance of D. J. Wells.

APPENDIX A: InSb ENERGY-BAND STRUCTURE IN A MAGNETIC FIELD

The structure of the conduction and valence bands in InSb in a magnetic field has been the subject of a number of studies. In analogy with Kane's³⁴ treatment of the zero-field case, Bowers and Yafet³⁵ modified the effective-mass theory of Luttinger and Kohn¹⁷ (LK) by including exactly the interaction between the conduction and valence bands neglecting only small terms arising from the lack of inversion symmetry in InSb.³⁴ They included, by perturbation theory to order k^2 , the effects of higher bands on the conduction-band energy levels and the magnetic susceptibility. Pidgeon and Brown¹⁸ in a similar approach evaluated both the conduction- and valence-band eigenvalues and the selection rules for optical interband absorption.

In this Appendix we give the eigenvectors for both the conduction and valence bands evaluated to lowest order in the magnetic field and in k_x , the momentum along the magnetic field direction. These eigenvectors are necessary in the evaluation of the spin-flip Raman-scattering cross section discussed in Sec. II A. As shown by LK the eigenfunctions can be expanded as

$$\Psi_{b,n,\sigma}(\vec{r}) = \sum_j e^{i k_y y} e^{i k_z z} \int d k_x e^{i k_x [x - (k_y / s)]}$$

$$\times c_j(b, n, \sigma) \varphi_{n_j}(k_x/\sqrt{s}) u_{j,0}(\vec{r}), \quad (\text{A1})$$

where b is a band index, n the Landau-level number, and σ the effective spin index. Here $s = eH/\hbar c$, φ_{n_j} are harmonic-oscillator eigenfunctions and the $u_{j,0}(\vec{r})$ are the $\vec{k}=0$ eigenstates in zero magnetic field, viz.,

$$\begin{aligned} u_{1,0}(\vec{r}) &= |c\alpha\rangle = |S\uparrow\rangle \\ u_{2,0}(\vec{r}) &= |h\alpha\rangle = (1/\sqrt{2})|(X+iY)\uparrow\rangle, \\ u_{3,0}(\vec{r}) &= |l\alpha\rangle = (1/\sqrt{6})|(X-iY)\uparrow + 2Z\uparrow\rangle, \\ u_{4,0}(\vec{r}) &= |d\alpha\rangle = (1/\sqrt{3})|(X-iY)\uparrow - Z\uparrow\rangle, \\ u_{5,0}(\vec{r}) &= |c\beta\rangle = |S\downarrow\rangle, \\ u_{6,0}(\vec{r}) &= |h\beta\rangle = (1/\sqrt{2})|(X-iY)\downarrow\rangle, \\ u_{7,0}(\vec{r}) &= |l\beta\rangle = (1/\sqrt{6})|(X+iY)\downarrow - 2Z\downarrow\rangle, \\ u_{8,0}(\vec{r}) &= |d\beta\rangle = (1/\sqrt{3})|(X+iY)\downarrow + Z\downarrow\rangle. \end{aligned} \quad (\text{A2})$$

Here S is the conduction-band function which transforms as an atomic s function; X , Y , and Z are valence-band functions that transform as atomic p functions. The labeling of the states in the middle column of (A2) indicates the zero-field bands to which they correspond; namely c —conduction band, h —heavy-hole band, l —light-hole band, and d —split-off band. The n_j are related to n and j by the following convention $n_1 = n_5 = n$, $n_2 = n_7 = n - 1$, $n_3 = n_4 = n_6 = n + 1$. The coefficients $c_j(b, n, \sigma)$ evaluated to first order in s and k_z , are given in Tables II and III.

The energies of these states are given in this lowest-order approximation by the parabolic-band expressions:

(i) conduction band:

$$E_{c,n,\sigma} = E_g + \frac{\hbar^2 k_z^2}{2m_c} + (n + \frac{1}{2}) \frac{\hbar^2 s}{m_c} \pm \frac{\hbar^2 s}{2m_c'}, \quad (\text{A3a})$$

$$\frac{1}{m_c} = \frac{2P^2}{3\hbar^2} \left(\frac{2}{E_g} + \frac{1}{E_g + \Delta} \right), \quad (\text{A3b})$$

$$\frac{1}{m_c'} = -\frac{2P^2}{3\hbar^2} \left(\frac{1}{E_g} - \frac{1}{E_g + \Delta} \right); \quad (\text{A3c})$$

(ii) heavy-hole band:

$$E_{h,n,\sigma} = 0; \quad (\text{A4})$$

(iii) light-hole band:

$$E_{l,n,\sigma} = \frac{\hbar^2 k_z^2}{2m_l} + (n + \frac{1}{2}) \frac{\hbar^2 s}{m_l} \pm \frac{\hbar^2 s}{2m_l'}, \quad (\text{A5a})$$

$$\frac{1}{m_l} = -\frac{4P^2}{3E_g \hbar^2}, \quad \frac{1}{m_l'} = \frac{2P^2}{3E_g \hbar^2}; \quad (\text{A5b})$$

(iv) spin-split-off band:

$$E_{d,n,\sigma} = -\Delta + \frac{\hbar^2 k_z^2}{2m_d} + (n + \frac{1}{2}) \frac{\hbar^2 s}{m_d} \pm \frac{\hbar^2 s}{2m_d'}, \quad (\text{A6a})$$

TABLE II. Eigenvectors in a magnetic field including finite k_z . See Appendix A for $n = -1$ levels.

$\varphi_n c\alpha\rangle$	$\varphi_{n-1} h\alpha\rangle$	$\varphi_{n+1} l\alpha\rangle$	$\varphi_{n+1} c\beta\rangle$	$\varphi_n l\beta\rangle$	$\varphi_n d\beta\rangle$
1	$-i \frac{P}{E_g} (sn)^{1/2}$	$\frac{P}{E_g} \left(\frac{s(n+1)}{3} \right)^{1/2}$	$-i \frac{P}{E_g + \Delta} \left(\frac{2s(n+1)}{3} \right)^{1/2}$	$\frac{2iPk_z}{\sqrt{6}E_g}$	$-i \frac{Pk_z}{\sqrt{3}(E_g + \Delta)}$
	$\left(\frac{s(n+1) + 2k_z^2}{s(4n+1) + 2k_z^2} \right)^{1/2}$	$\left(\frac{1}{s(n+1) + 2k_z^2} \right)^{1/2}$	$-\left(\frac{6sk_z^2 n}{s(4n+1) + 2k_z^2} \frac{1}{s(n+1) + 2k_z^2} \right)^{1/2}$	$\left(\frac{2k_z^2}{s(4n+1) + 2k_z^2} \right)^{1/2}$	$\left(\frac{1}{s(4n+1) + 2k_z^2} \right)^{1/2}$
	$\left(\frac{3sn}{s(4n+1) + 2k_z^2} \right)^{1/2}$	$\left(\frac{s(n+1)}{s(4n+1) + 2k_z^2} \right)^{1/2}$	1	$\frac{iPk_z}{\sqrt{3}(E_g + \Delta)}$	$ c, n, \alpha\rangle$
	$-i \frac{P}{E_g} \left(\frac{s(4n+1) + 2k_z^2}{3} \right)^{1/2}$	$-\left(\frac{P}{E_g} \left(\frac{2s(n+1)}{3} \right)^{1/2} \right)$			$ h, n, \alpha\rangle$ $n \geq 1$
	$-i \frac{P}{E_g + \Delta} \left(\frac{2s(n+1)}{3} \right)^{1/2}$				$ l, n, \alpha\rangle$
					$ d, n, \alpha\rangle$

$$\frac{1}{m_d} = \frac{1}{m_d'} = -\frac{2P^2}{3(E_g + \Delta)\hbar^2} \quad (\text{A6b})$$

These results are correct for $n \geq 0$. For $n = -1$ there are valence-band states that arise because of the mixing of φ_{n+1} and φ_{n-1} harmonic-oscillator functions in the valence band. These states and their energy levels are listed below:

(i) $n = -1$ eigenstates and eigenvalues:

$$|l, -1, \alpha\rangle = \left(\frac{3s}{3s + 2k_z^2}\right)^{1/2} \varphi_0 |l\alpha\rangle + \left(\frac{2k_z^2}{3s + 2k_z^2}\right)^{1/2} \varphi_1 |h\beta\rangle, \quad E_{l,-1,\alpha} = 0, \quad (\text{A7})$$

$$|d, -1, \alpha\rangle = \varphi_0 |d\alpha\rangle + i \frac{P}{E_g + \Delta} \frac{k_z}{\sqrt{3}} \varphi_0 |c\beta\rangle,$$

$$E_{d,-1,\alpha} = \frac{\hbar^2 k_z^2}{2m_d} - \Delta, \quad (\text{A8})$$

$$|l, -1, \beta\rangle = \varphi_0 |h\beta\rangle, \quad E_{l,-1,\beta} = 0. \quad (\text{A9})$$

APPENDIX B: ALTERNATE DERIVATION OF EFFECTS OF ORBITAL COLLISIONS ON LINE SHAPE

In this Appendix an alternate derivation of the effects of orbital collisions on the spin-flip Raman-scattering line shape is presented. The model presented here is based on a real-time, rather than a frequency-space, approach to the collision problem which gives additional insight into the physics involved.

The calculation follows the time evolution of the scattering line shape due to a single-spin excitation initiated at $t=0$. The calculation is carried out for the quantum limit; $T=0$ is assumed and the band-edge value of the spin-flip matrix element is used. The calculation can readily be extended to include the effects of finite temperature and partial population of the higher Landau sublevels. The model is characterized by two phenomenological collision times (see Sec. II B):

(i) τ_s , a time that characterizes those processes that either relax the spin excitation or randomly interrupt the phase of the electron spin precession and (ii) τ_p , a time that characterizes the orbital relaxation of this spin excitation. This relaxation corresponds to a collision which alters the k_z state of the spin excitation but does not affect the phase of the spin precession. Collisions are assumed to be independent Poisson-distributed random events. The method of the calculation is to evaluate the autocorrelation function of the random variable $x(t)$ that represents the scattering from a single excited electron. The line shape is then evaluated by obtaining the power spectral density which is given by the Fourier transform of this autocorrelation

TABLE III. Eigenvectors in a magnetic field including finite k_z . See Appendix A for $n = -1$ levels.

$\varphi_{n-1} c\alpha\rangle$	$\varphi_n l\alpha\rangle$	$\varphi_n c\beta\rangle$	$\varphi_{n+1} h\beta\rangle$	$\varphi_{n-1} l\beta\rangle$	$\varphi_{n-1} d\beta\rangle$
$\frac{-iPk_z}{\sqrt{3(E_g + \Delta)}}$	$\frac{iPk_z}{\sqrt{3(E_g + \Delta)}}$	1	$-i \frac{P}{E_g} [s(n+1)]^{1/2}$	$-i \frac{P}{E_g} \left(\frac{sn}{3}\right)^{1/2}$	$-i \frac{P}{E_g + \Delta} \left(\frac{2sn}{3}\right)^{1/2}$
$\left(\frac{6s(n+1)k_z^2}{s(4n+3) + 2k_z^2} \frac{1}{sn + 2k_z^2}\right)^{1/2}$	$\left(\frac{sn + 2k_z^2}{s(4n+3) + 2k_z^2}\right)^{1/2}$	$- \left(\frac{sn + 2k_z^2}{s(4n+3) + 2k_z^2}\right)^{1/2}$	$\left(\frac{3s^2 n(n+1)}{s(4n+3) + 2k_z^2} \frac{1}{sn + 2k_z^2}\right)^{1/2}$	$\left(\frac{sn}{s(4n+3) + 2k_z^2}\right)^{1/2}$	$\left(\frac{1}{s(4n+3) + 2k_z^2}\right)^{1/2}$
$\left(\frac{2k_z^2}{s(4n+3) + 2k_z^2}\right)^{1/2}$	$-i \frac{P}{E_g} \left(\frac{s(4n+3) + 2k_z^2}{3}\right)^{1/2}$	$-i \frac{P}{E_g} \left(\frac{2sn}{3}\right)^{1/2}$			
$\frac{-iPk_z}{\sqrt{3(E_g + \Delta)}}$					1
					$n \geq 1$

function. The techniques used in the calculation follow, to a large extent, the method outlined by Margenau and Lewis.³⁶

For the case of spin-flip Raman scattering, the time function of interest is of the form

$$x(t) = F e^{i\varphi(t)}, \quad (\text{B1})$$

where F is the time-independent driving term and $\varphi(t)$ is the total accumulated phase of the electron spin precession given by

$$\varphi(t) = \int_0^t \omega_s(k_z(t')) dt'. \quad (\text{B2})$$

Because of orbital collisions, k_z is a function of time. If these collisions were not present, the evaluation of $\varphi(t)$ and subsequently the power spectral density would be straightforward and would yield the simple inhomogeneously broadened line shapes of (2.22). Alternatively, if there were no inhomogeneous broadening mechanisms, as would be the case for parabolic bands in a geometry in which there was no Doppler shift, the orbital collisions would have no effect on the line shape which would be a simple Lorentzian with a linewidth (full width at half-height) of $2/\tau_s$. In order to simplify the notation somewhat, the subscript on k will be dropped and the time dependence will be indicated by the abbreviated notations k_t and k_i , where k_i is the value of k at time τ_i .

The autocorrelation function $R(\tau)$ of the function $x(t)$ can be evaluated as an average over an ensemble of electrons, e.g.,

$$\begin{aligned} R(\tau) &= E[x(t+\tau)x^*(t)] \\ &= |F|^2 E\{\exp[-i \int_t^{t+\tau} \omega_s(k_i) dt']\}, \end{aligned} \quad (\text{B3})$$

where E denotes the ensemble average and the band-edge approximation has been made for the spin-flip matrix element. Using a slightly generalized version of (B2), this can be written as

$$R(\tau) = |F|^2 \int_{-\infty}^{\infty} p_\tau(\varphi) e^{-i\varphi} d\varphi, \quad (\text{B4})$$

where $p_\tau(\varphi)$ is the probability density of accumulating the phase φ in the time τ . $p_\tau(\varphi)$ is independent of t because the collision process is assumed to be a stationary random process, and is given by a sum over the probability densities of all possible time evolutions of a spin excitation in the time interval τ which accumulate the correct phase with a given number of collisions, e.g.,

$$p_\tau(\varphi) d\varphi = \sum_{n=0}^{\infty} \tilde{p}_{n,\tau}(\varphi) d\varphi \quad (\text{B5})$$

where $\tilde{p}_{n,\tau}(\varphi)$ is the probability density of accumulating the phase φ in the time τ while undergoing n collisions. Similarly, $p_{n,\tau}(\varphi)$ can be evaluated as a sum over all possible time evolutions which accumulate the correct phase

$$\begin{aligned} p_{n,\tau}(\varphi) &= \int_{-\infty}^{\infty} d\varphi_1 \int_0^{\infty} d\tau_1 p(\varphi_1, \tau_1) \cdots \\ &\times \int_{-\infty}^{\infty} d\varphi_n \int_0^{\infty} d\tau_n p(\varphi_n, \tau_n) \\ &\times \int_{-\infty}^{\infty} d\varphi_{n+1} \int_0^{\infty} d\tau_{n+1} P_0(\varphi_{n+1}, \tau_{n+1}) \\ &\times \delta\left(\varphi - \sum_1^{n+1} \varphi_i\right) \delta\left(\tau - \sum_1^{n+1} \tau_i\right), \end{aligned} \quad (\text{B6})$$

where the δ functions assure that the sum of the phase steps between collisions is φ and the sum of the time intervals is τ . Note that there are $n+1$ phase steps for a path with n collisions. In the above, $p(\varphi_i, \tau_i) d\varphi_i d\tau_i = p(k_i, \tau_i) dk_i d\tau_i$ is the probability density that the electron remains in the k -state k_i for the time interval τ_i such that the phase step is $\varphi_i = \omega_s(k_i)\tau_i$, and $P_0(\varphi_{n+1}, \tau_{n+1}) d\varphi_{n+1} = P_0(k_{n+1}, \tau_{n+1}) dk_{n+1} d\tau_{n+1}$ is the probability density that there are no collisions in the time interval τ_{n+1} and that the phase step in this interval is $\varphi_{n+1} = \omega_s(k_{n+1})\tau_{n+1}$. The δ functions can be replaced by their expressions in the Dirichlet representation, e.g.,

$$\delta\left(\varphi - \sum_1^{n+1} \varphi_i\right) = \frac{1}{2\pi} \int_{-\infty}^{\infty} dy \exp\left[iy\left(\varphi - \sum_1^{n+1} \varphi_i\right)\right]. \quad (\text{B7})$$

Substituting (B7) into (B6), writing out the expression for the φ_i , and reversing the order of integration, results in the expression

$$\begin{aligned} p_{n,\tau}(\varphi) &= \frac{1}{(2\pi)^2} \int_{-\infty}^{\infty} dx \int_{-\infty}^{\infty} dy e^{ix\tau + iy\varphi} \\ &\times \left(\prod_{i=1}^n \int dk_i \int d\tau_i p(k_i, \tau_i) \exp[-i\omega_s(k_i)\tau_i - ix\tau_i] \right) \\ &\times \int dk_{n+1} \int d\tau_{n+1} P_0(k_{n+1}, \tau_{n+1}) \\ &\times \exp[-i\omega_s(k_{n+1})\tau_{n+1} y - ix\tau_{n+1}]. \end{aligned} \quad (\text{B8})$$

Using the probability distributions of a Poisson process, the τ' integrations can readily be carried out with the result

$$p_{n,\tau}(\varphi) = \frac{\tau_p}{(2\pi)^2} \int_{-\infty}^{\infty} dx \int_{-\infty}^{\infty} dy e^{i(x\tau + y\varphi)} \left\langle \frac{1}{1 + i\omega_s(k)y\tau_p} \right\rangle^{n+1}, \quad (\text{B9})$$

where the notation $\langle G(k) \rangle = \int_{-\infty}^{\infty} p(k)G(k) dk$ has been used and $p(k)$ is the probability distribution of k values after a τ_p collision. This result can be used along with (B4) and (B5) to evaluate the power spectral density

$$S(\omega) = 2 \operatorname{Re} \left[\frac{1}{2\pi} \int_{-\infty}^{\infty} dx \left(\tau_p \sum_{n=0}^{\infty} \left\langle \frac{1}{1 + i\omega_s(k) + ix\tau_p} \right\rangle^{n+1} \right) \right]$$

$$i[\omega - \omega_s(k) - x - i/\tau_s] \Big] \quad (\text{B10})$$

where the order of integration has again been reversed and the Fourier-transform integration has already been performed. There is a simple pole at $x = \omega - \omega_s - i/\tau_s$ and a complicated branch cut along $x = -\omega_s(k) + i/\tau_p$. The function is well behaved everywhere else in the complex plane and the integral can be readily evaluated. The result

is

$$S(\omega) = 2 \operatorname{Im} \left[\left\langle \frac{1}{\omega_s(k) - \omega + i/\tau} \right\rangle \right. \\ \left. \left(1 - \frac{i}{\tau_p} \left\langle \frac{1}{\omega_s(k) - \omega + i/\tau} \right\rangle \right) \right], \quad (\text{B11})$$

where $1/\tau = 1/\tau_s + 1/\tau_p$.

This expression is identical in form with (2.21).

[†]This work was sponsored by the Department of the Air Force.

^{*}Present address: Texas Instruments, Inc., Dallas, Texas.

¹C. K. N. Patel and E. D. Shaw, Phys. Rev. Lett. **24**, 451 (1970); Phys. Rev. B **3**, 1279 (1971).

²A. Mooradian, S. R. J. Brueck, and F. A. Blum, Appl. Phys. Lett. **17**, 481 (1970); S. R. J. Brueck and A. Mooradian, Appl. Phys. Lett. **18**, 229 (1971).

³R. L. Aggarwal, B. Lax, C. E. Chase, C. R. Pidgeon, D. Limbert, and F. Brown, Appl. Phys. Lett. **18**, 383 (1971).

⁴R. L. Allwood, R. B. Dennis, S. D. Smith, B. S. Wherrett, and R. A. Wood, J. Phys. C **4**, L163 (1971); R. L. Allwood, R. B. Dennis, R. G. Mellish, S. D. Smith, B. S. Wherrett, and R. A. Wood, J. Phys. C **4**, L126 (1971).

⁵J. F. Scott, T. C. Damen, and P. A. Fleury, Phys. Rev. B **6**, 3856 (1972).

⁶Portions of this work were reported in preliminary publications: S. R. J. Brueck, Ph.D. thesis (MIT, 1971) (unpublished); S. R. J. Brueck and A. Mooradian, Phys. Rev. Lett. **28**, 161 (1972); S. R. J. Brueck and F. A. Blum, Phys. Rev. Lett. **28**, 1458 (1972).

⁷R. E. Slusher, C. K. N. Patel, and P. A. Fleury, Phys. Rev. Lett. **18**, 530 (1967).

⁸C. K. N. Patel and R. E. Slusher, Phys. Rev. **167**, 413 (1968).

⁹P. A. Fleury and J. F. Scott, Phys. Rev. B **3**, 1979 (1971); T. W. Walker, C. W. Litton, D. C. Reynolds, T. C. Collins, W. A. Wallace, J. H. Gorrell, and K. C. Jungling, in Proceedings of the Eleventh International Conference on the Physics of Semiconductors, Warsaw, Poland, 1972 (unpublished).

¹⁰C. K. N. Patel and R. E. Slusher, Phys. Rev. **177**, 1200 (1969).

¹¹C. K. N. Patel and K. H. Yang, Appl. Phys. Lett. **18**, 491 (1971).

¹²P. A. Wolff, Phys. Rev. Lett. **16**, 255 (1966).

¹³Y. Yafet, Phys. Rev. **152**, 848 (1966).

¹⁴G. B. Wright, P. L. Kelley, and S. H. Groves, in *Light Scattering Spectra of Solids*, edited by G. B. Wright (Springer-Verlag, New York, 1969), pp. 335-343.

¹⁵B. S. Wherrett and P. G. Harper, Phys. Rev. **183**, 692 (1969).

¹⁶V. P. Makarov, Zh. Eksp. Teor. Fiz. **55**, 704 (1968) [Sov. Phys.-JETP **28**, 336 (1969)].

¹⁷J. M. Lutinger and W. Kohn, Phys. Rev. **97**, 869 (1955).

¹⁸C. R. Pidgeon and R. N. Brown, Phys. Rev. **146**, 575 (1966).

¹⁹S. R. J. Brueck, Ph.D. thesis (MIT, 1971) (unpublished).

²⁰R. L. Aggarwal, B. Lax, C. R. Pidgeon, and D. Limbert, in *Proceedings of the International Conference on Light Scattering in Solids* (Flammarion, Paris, 1971).

²¹R. W. Davies, Phys. Rev. B (to be published).

²²R. W. Davies and F. A. Blum, Phys. Rev. B **3**, 3321 (1971).

²³Y. Yafet, in *Solid State Physics*, edited by F. Seitz and D. Turnbull (Academic, New York, 1963) Vol. 14; W. G. Clark and G. Feher, Phys. Rev. Lett. **10**, 134 (1963); R. A. Isaacson, Phys. Rev. **169**, 313 (1968); K. Sugihara, J. Phys. Soc. Jap. **28**, 402 (1970).

²⁴G. Bemski, Phys. Rev. Lett. **4**, 62 (1960); R. L. Bell, Phys. Rev. Lett. **9**, 521 (1962); E. M. Gershenzon, N. M. Perin, and M. S. Fogel'son, Fiz. Tverd. Tela **10**, 2880 (1968) [Sov. Phys.-Solid State **10**, 2278 (1969)]; J. Konopka, Phys. Rev. Lett. **24**, 666 (1970); B. D. McCombe and R. J. Wagner, Phys. Rev. B **4**, 1285 (1971).

²⁵Y. C. Auyang and P. A. Wolff (private communication); Y. C. Auyang, Ph.D. thesis (MIT, 1971) (unpublished).

²⁶See, for example, C. P. Slichter, *Principles of Magnetic Resonance* (Harper, New York, 1964); and also A. Abragam, *The Principles of Nuclear Magnetism* (Clarendon, Oxford, 1961).

²⁷R. M. Osgood, W. E. Eppers, and E.R. Nichols, IEEE J. Quantum Electron. **6**, 145 (1970).

²⁸T. M. Quist, Proc. IEEE **56**, 1212 (1968).

²⁹E. J. Johnson and D. H. Dickey, Phys. Rev. B **1**, 2676 (1970).

³⁰C. R. Pidgeon, D. L. Mitchell, and R. N. Brown, Phys. Rev. **154**, 737 (1967).

³¹B. D. McCombe and R. J. Wagner, Phys. Rev. B **4**, 1285 (1971).

³²S. H. Groves, C. R. Pidgeon, A. W. Ewald, and R. J. Wagner, J. Phys. Chem. Solids **31**, 2031 (1970).

³³A. Mooradian and H. Y. Fan, Phys. Rev. **148**, 873 (1966).

³⁴E. O. Kane, J. Phys. Chem. Solids **4**, 249 (1957).

³⁵R. Bowers and Y. Yafet, Phys. Rev. **115**, 1165 (1959); see also Y. Yafet, Phys. Rev. **152**, 858 (1966).

³⁶H. Margenau and M. Lewis, Rev. Mod. Phys. **31**, 569 (1959).